NACA RM E51H17

NACA

RESEARCH MEMORANDUM

AERODYNAMIC CHARACTERISTICS OF A SLENDER CONE-CYLINDER BODY OF REVOLUTION AT A MACH NUMBER OF 3.85

By John R. Jack

Lewis Flight Propulsion Laboratory
Cleveland, Ohio

NATIONAL ADVISORY COMMITTEE
FOR AERONAUTICS

WASHINGTON
November 5, 1951

NATIONAL ADVISORY COMMITTEE FOR AERONAUTICS

RESEARCH MEMORANDUM

AERODYNAMIC CHARACTERISTICS OF A SLENDER CONE-CYLINDER BODY OF REVOLUTION AT A MACH NUMBER OF 3.85

By John R. Jack

SUMMARY

An experimental investigation to determine the aerodynamic characteristics of a slender body of revolution having a conical forebody and a cylindrical afterbody was conducted in the NACA Lewis 2- by 2-foot supersonic wind tunnel. Pressure distributions, viscous drag, and three component forces were measured at a Mach number of 3.85 for an angle of attack range of 0° to 10° and for a Reynolds number of 3.85×10^{6}.

The experimental pressure distributions due to angle of attack on the bottom surface of the conical forebody of the model agreed well with theory for small angles of attack. On the top surface of the model, experiment and theory agreed very well on the conical forebody. For the cylindrical afterbody, however, the agreement was good only for small angles of attack. The base-pressure coefficient increased and then decreased as the angle of attack was increased. The maximum base-pressure coefficient was obtained at about 4° angle of attack.

A breakdown of the measured total drag into its components at zero angle of attack showed that the fore-pressure drag was 34 percent, the base-pressure drag was 40 percent, and the skin-friction drag was 26 percent of the total drag. A semiempirical theory for estimating forces and moments predicted trends similar to the experimental ones, but underestimated the increment in drag coefficient due to angle of attack, the lift coefficient, and the pitching-moment coefficient.

INTRODUCTION

The linearized potential theory adequately predicts the pressure distributions for low supersonic Mach numbers and for zero angle of attack, but fails to predict accurately the incremental pressure distributions and over-all forces resulting from angle of attack. The

body forces experienced at low supersonic Mach numbers are estimated more successfully by the semiempirical method of reference 1, which accounts somewhat for the viscous effects. The aerodynamic characteristics of a slender square-based body of revolution at a Mach number of 3.12 have been compared with existing theories for a range of angles of attack and Reynolds numbers in reference 2. The investigation presented herein was conducted at the NACA Lewis laboratory at a Mach number of 3.85 to evaluate further the existing theories and to complement the basic aerodynamic data available at high Mach numbers.

Pressure distributions and the forces acting on a cone-cylinder-type body were determined experimentally and compared with linearized potential theory and the semiempirical theory of reference 1. A boundary-layer study was made at several axial stations to evaluate the effects of viscosity and to provide a better correlation of experimental data.

APPARATUS AND PROCEDURE

The investigation was made in the NACA Lewis 2- by 2-foot supersonic tunnel, which is a nonreturn-type tunnel having a Reynolds number per foot of 1.1×10^6 and a test section Mach number of 3.85 ± 0.04. A total temperature of approximately 200° F and a specific humidity of 8.0×10^{-4} pounds of water per pound of dry air or less were maintained for all runs. This specific humidity insured negligible condensation effects.

A photograph of the body is shown in figure 1 and its dimensions and instrumentation are given in figure 2. The body used for the pressure distributions was turned from steel and polished to a 16-microinch finish. The pertinent geometric parameters of the model are given in the following table:

Half-angle of cone, ϵ, deg	4.77
Body length, l, in.	42
Fineness ratio, F	12
Volume of body, V, cu in.	269.39
Wetted area, A_w, sq in.	346.20
Frontal area, A_F, sq in.	9.62
Base area, A_b, sq in.	9.62
Plan-form area, A_p, sq in.	110.25
Maximum body diameter, d_m, in.	3.50

(All symbols are defined in the appendix.)

The static-pressure orifices were arranged in five rows and were located at the stations given in figure 2. The boundary-layer data for zero angle of attack and for axial stations upstream of the base were

obtained with the probe pictured in figure 3(a). The data for the base station were obtained with the rake shown in figure 3(b).

The model was supported from its base by a sting extending upstream from a vertical strut mounted to the top of the tunnel. Interference of the sting with the base pressures at zero angle of attack was minimized by designing the sting on the basis of the data presented in reference 3.

The force model was the same as the pressure-distribution model except that it was turned from aluminum and had a 6-microinch finish. The model was rigidly connected to a three-component strain gage that was attached to the sting-strut combination. Because the strain gage was mounted internally, no aerodynamic tare corrections were necessary.

REDUCTION OF DATA AND METHODS OF COMPUTATION

In the reduction of the pressure data, the free-stream static pressure was determined by averaging the pressures measured by several static orifices located on the tunnel walls opposite the tip of the model. The increments of pressure coefficient due to angle of attack were obtained by subtracting the values measured at zero angle of attack from those measured at angle of attack.

Total-pressure measurements in the boundary layer were evaluated using the Rankine-Hugoniot equation with the assumptions that the total temperature in the flow field remained constant and that the static pressure remained constant along radial lines through the boundary layer. Skin-friction coefficients were calculated using the momentum equation

$$C_{D,f} = \frac{2\pi}{q_0 A_w}\left[\int_0^s \frac{d}{ds}\left(r\rho_1 u_1^2 \theta\right) ds - \int_0^s r\delta^* \frac{dp}{ds}\, ds\right] \qquad (1)$$

where

$$\theta = \frac{1}{\rho_1 u_1^2}\int_0^\infty \rho u(u_1 - u)\, dy$$

$$\delta^* = \frac{1}{\rho_1 u_1}\int_0^\infty (\rho_1 u_1 - \rho u)\, dy$$

and

s distance measured along surface of body

y distance measured normal to body surface

The theoretical pressure-distribution curves were calculated from the following expansion of the exact expression for the pressure coefficient:

$$C_p = \left(1 - \frac{U^2}{U_0^2}\right) + \left(\frac{M_0}{2}\right)^2 \left(1 - \frac{U^2}{U_0}\right)^2 + \cdots \qquad (2)$$

The perturbation velocities associated with zero angle of attack were computed using the numerical method of reference 4, whereas the perturbation velocities associated with angle of attack were estimated using slender-body theory (see, for example, references 1 or 5). The slender-body theory is not expected to be valid in the vicinity of a discontinuity of surface slope. Equation (2) is usually approximated by

$$C_p = \left(1 - \frac{U^2}{U_0^2}\right)$$

$$= -\frac{2}{U_0}\left(\frac{\partial \phi}{\partial x}\right)_{\alpha=0} - \left(\frac{dr}{dx}\right)^2 + 4\,\alpha \cos\theta \frac{dr}{dx} + \alpha^2 (1 - 4 \sin^2\theta) \qquad (3)$$

where $\left(\frac{\partial \phi}{\partial x}\right)_{\alpha=0}$ is the axial perturbation velocity for zero angle of attack. Comparison of equations (2) and (3) shows that the pressure distributions given by the two relations are enough different to warrant considering equation (2). Consequently, equations (2) and (3) have been compared on the conical part of the body for three angles of attack.

Theoretical force coefficients were calculated by the method of reference 1, which accounts to some extent for the viscous effects. The equations given in reference 1 for the force and moment coefficients are

$$\Delta C_D = \alpha^2 + \eta\, C_{d,c} \frac{A_P}{A_F} \alpha^3 \qquad (4)$$

$$C_L = 2\alpha + \eta\, C_{d,c} \frac{A_P}{A_F} \alpha^2 \qquad (5)$$

$$C_M = 2\frac{V}{A_F l}\alpha + \eta\, C_{d,c}\frac{A_P}{A_F}\left(\frac{l-x_P}{l}\right)\alpha^2 \qquad (6)$$

where x_P is the centroid of the plan area, η is the ratio of the drag coefficient of a circular cylinder of finite length to that of a cylinder of infinite length, and $C_{d,c}$ is the section drag coefficient of a circular cylinder per unit length. The values of η and $C_{d,c}$ selected from reference 1 are 0.70 and 1.20, respectively, and correspond to conditions at the lower angles of attack.

RESULTS AND DISCUSSION

The experimental results consist of pressure distributions on the body surface, boundary-layer surveys for several axial stations, and force measurements. These results are discussed both for zero angle of attack and for angle of attack.

Forebody Pressure Distribution

Zero angle of attack. - The experimental variation of the pressure coefficient with axial position on the body is presented in figure 4(a) for zero angle of attack. Theoretical curves computed from equations (2) and (3) are compared with the experimental data.

The agreement between experiment and theory on the conical forebody is poor; however, the difference between experiment and theory is small for the cylindrical afterbody. Equation (2) reduces the difference between experiment and theory, but not by a great amount. The exact conical value is presented in figure 4(a) for comparison and it also falls below the experimental values. The disagreement between the exact conical value and the experimental values is attributed to a Reynolds number effect of the same type as that obtained in reference 2; that is, as the Reynolds number increases, the agreement between experiment and theory improves considerably. It was impossible to account for this discrepancy by adding the boundary-layer displacement thickness to the body contour. The effect of adding the boundary-layer displacement thickness to the body contour was to increase the conical half-angle by approximately 0.09°, which increased the cone pressure coefficient to approximately 0.025.

Angle of attack. - The axial pressure distributions along the top and bottom of the model are presented in figure 4(b) for two angles of attack. On the bottom of the conical forebody, the agreement between

equation (2) and experiment is much better than the agreement given by equation (3). Because the difference between equations (2) and (3) is very small for the cylindrical afterbody and for the top of the conical forebody ($\theta = 180^\circ$), no comparison has been made.

The pressure-coefficient increments due to angle of attack, as determined from figure 4, are compared in figure 5 with equations (2) and (3). Again, a comparison between equations (2) and (3) has not been made for $\theta = 180^\circ$ or for the cylindrical afterbody. On the bottom surface of the conical forebody ($\theta = 0^\circ$), the qualitative agreement between theory and experiment appears to be good for an angle of attack of 3° but not for an angle of attack of 10°. Actually, theory underestimates experiment by approximately 20 percent for both angles of attack. The agreement for $\theta = 0^\circ$ on the cylindrical portion of the body is poor for both angles of attack. On the top surface of the conical forebody ($\theta = 180^\circ$), experiment and theory agree very well; for the cylindrical part of the body, the agreement is good for an angle of attack of 3° but not for an angle of attack of 10°. The difference between experiment and theory for an angle of attack of 10° is attributed mainly to cross-flow separation.

Experimental pressure distributions as functions of the meridian angle around the body are given in figure 6 for three axial stations. From figure 6 the pressure-coefficient increments due to angle of attack were obtained and plotted in figure 7. For the 11-inch axial station (fig. 7(a)) and an angle of attack of 3°, theory agrees fairly well with experiment; however, for all other stations the agreement is poor. Equation (2) gives better agreement than equation (3), but there is still a large difference between experiment and theory. On the cone and in the vicinity of the break between the cone and the cylinder, the discrepancy between the theoretical and experimental curves may be attributed to the inadequacy of linearized potential theory; whereas further downstream on the cylindrical section, the discrepancy may be attributed to the inability of linearized theory to account for the effect of the viscous cross flow.

Base-Pressure Coefficients

The effect of angle of attack on the base-pressure coefficient is presented in figure 8. The variation of the base-pressure coefficient with angle of attack is of the same type as that obtained in reference 2 for a Reynolds number of 4×10^6; that is, the base-pressure coefficient increases to a maximum near an angle of attack of $\pm 4.0^\circ$ and then decreases as the angle of attack is increased. The broken line between the data at an angle of attack of $\pm 3^\circ$ is used to indicate that the true variation of the pressure coefficient in this region is unknown. This behavior is associated with the movement of the transition region with increasing angle of attack (reference 2).

Boundary Layer and Skin Friction

In order to complete the investigation of the component drag forces contributing to the total drag of the body at zero angle of attack, friction-drag coefficients were obtained from the experimentally determined displacement and momentum thicknesses at several axial stations. The displacement and momentum thickness distributions are presented in figure 9. The momentum thickness distribution shows no rapid changes such as those associated with transition, thereby indicating that the flow was completely laminar.

The experimental mean skin-friction coefficients $C_{D,f}$ are compared in figure 10 with the theoretical laminar skin-friction coefficients for an insulated flat plate (reference 6) and with the laminar skin-friction coefficients derived for a cone (reference 7). These skin-friction coefficients based on wetted area are given respectively by

$$C_{D,f} = \frac{1.257}{\sqrt{Re}} \tag{7}$$

and

$$C_{D,f} = \frac{2}{\sqrt{3}} \frac{1.257}{\sqrt{Re}} \tag{8}$$

Equation (7) agrees with the numerical results of reference 8 to within 2 percent.

Although a quantitative comparison between the measured body-friction coefficients and the flat-plate coefficients is questionable, a comparison of the measured values and those predicted by equation (8) appears reasonable. As figure 10 shows, the agreement between the coefficients measured on the conical forebody and the theoretical cone coefficients is good. The one point not in good agreement ($Re = 1.90 \times 10^6$) was 0.25 inch upstream of the junction between the cone and the cylinder and was probably influenced by this break. The coefficients measured on the cylindrical afterbody are lower than the theoretical cone values and approach the flat-plate values. This is to be expected and may be predicted since the mean skin-friction coefficient is continuous at the break between the cone and the cylinder. If the cylinder were provided with a hypothetical leading edge with sufficient length to provide a friction drag equal to that of the cone, the skin-friction-drag coefficient for the cone-cylinder combination may then be obtained by treating the cone-cylinder as an extended cylinder. The equation obtained by following this procedure is

$$C_{D,f}\ (\text{cone-cylinder combination}) = \frac{C_{D,f(\text{cone})}}{\frac{2}{\sqrt{3}}\left(1 - \frac{1}{4}\frac{x_1}{x}\right)^{1/2}} \tag{9}$$

where x_1 is the length of the conical forebody. The agreement between equation (9) and the coefficients measured on the cylindrical afterbody is good (fig. 10).

The effect of pressure gradient on the skin-friction coefficients was evaluated by calculating $C_{D,f}$ with both terms of equation (1) and with just the first term. The effect of the pressure gradient is negligible.

Force Measurements

The total-drag coefficient and the increment in drag due to angle of attack are plotted in figure 11(a). The increment in drag due to angle of attack is compared with the theortical curve obtained by the method of reference 1. This comparison shows that the method of reference 1 greatly underestimates the experimental values.

For zero angle of attack, a summation of the drag components shows the fore-pressure drag to be 34 percent, the base-pressure drag 40 percent, and the skin-friction drag 26 percent of the total drag. Very little difference occurred between the summation of the components and the total-drag coefficient obtained with the force model.

The variation of the lift coefficient with angle of attack is presented in figure 11(b). The calculated variations of the lift coefficient obtained from linearized theory and reference 1 are also presented in figure 11(b). The method of reference 1 ($C_{d,c} = 1.2$) predicts the variation more accurately than potential theory, but it still underestimates the experimental values by more than 40 percent at the higher angles of attack.

For the present investigation, the maximum cross-flow Reynolds number is 55,700, which is below the critical Reynolds number for a circular cylinder. At high angles of attack, however, the cross-flow Mach numbers from which the value of $C_{d,c}$ is determined fall in a region where $C_{d,c}$ is steadily increasing from a value of 1.2 (reference 1). The variation of lift coefficient determined with a variable $C_{d,c}$, corresponding to the cross-flow Mach numbers obtained for each angle of attack, is given in figure 11(b). The trend of the experimental lift-coefficient variation is better approximated at the higher angles of attack by a variable $C_{d,c}$.

The variation of the pitching-moment coefficient with angle of attack is given in figure 11(c). A comparison of the experimental values with those predicted by potential theory and the method of reference 1 shows

that for an angle of attack of 10° the method of reference 1 underestimates the absolute value by 31 percent and potential theory underestimates the absolute value by 64 percent. Because the slopes of the lift curve and the pitching-moment curve varied in such a manner as to keep the ratio of the two constant for all angles of attack, the position of the center of pressure remained relatively constant (fig. 11(d)). For all angles of attack, the method of reference 1 predicted a center of pressure approximately 2 diameters upstream of the experimental center of pressure.

SUMMARY OF RESULTS

The aerodynamic characteristics of a slender cone-cylinder body of revolution were investigated in the NACA Lewis 2- by 2-foot wind tunnel at a Mach number of 3.85. A summary of the results follows:

1. The agreement between the experimental and theoretical pressure distributions on the conical forebody for zero angle of attack was poor; however, there was very little difference between experiment and theory on the cylindrical afterbody.

2. The experimental pressure distributions due to angle of attack on the bottom surface of the conical forebody of the model agreed well with theory for small angles of attack. On the top surface of the model, experiment and theory for the conical part of the body agreed very well with theory. For the cylindrical part of the body, the agreement was good only for an angle of attack of 3° and the top surface of the model. Closer agreement between experiment and theory was obtained by adding an additional term to the series expansion for the pressure coefficient.

3. The base-pressure coefficient first increased and then decreased as the angle of attack was increased. The maximum base-pressure coefficient was obtained at about $\pm 4.0°$ angle of attack.

4. The measured mean skin-friction coefficients on the conical forebody agreed well with theoretical values obtained for laminar flow over cones.

5. A separation of the measured total drag into components at zero angle of attack showed that the fore-pressure drag was 34 percent, the base-pressure drag was 40 percent, and the skin-friction drag 26 percent of the total drag.

6. A semiempirical theory predicted trends similar to the experimental trends, but it underestimated the increment in drag coefficient due to angle of attack, the lift coefficient, and the pitching-moment coefficient.

Lewis Flight Propulsion Laboratory
National Advisory Committee for Aeronautics
Cleveland, Ohio

APPENDIX - SYMBOLS

The following symbols are used in this report:

A_b base area

A_F frontal area

A_P plan-form area

A_w wetted area

C_D drag coefficient, $D/q_0 A_F$

ΔC_D increment of drag coefficient due to angle of attack

C_p pressure coefficient, $(p-p_0)/q_0$

$C_{p,\alpha}$ pressure coefficient increment due to angle of attack

C_L lift coefficient, $L/q_0 A_F$

C_M pitching-moment coefficient, $M/q_0 A_F l$

D drag

d body diameter

F fineness ratio

L lift force

l body length

M pitching moment

M_0 free-stream Mach number

p static pressure

q dynamic pressure, $(\gamma/2)p_0 M_0^2$

Re Reynolds number, $\rho_0 U_0 l/\mu$

Re_x Reynolds number based on distance from nose of body

U total velocity, $\sqrt{v_x^2 + v_r^2 + v_\theta^2}$

U_0 free-stream velocity

u velocity in boundary layer

V volume of body

v_r radial velocity component

v_x axial velocity component

v_θ tangential velocity component

x,r,θ cylindrical coordinates

α angle of attack

γ ratio of specific heats, 1.40

δ^* displacement thickness, $\frac{1}{\rho_1 u_1}\int_0^\infty (\rho_1 u_1 - \rho u)\, dy$

θ momentum thickness, $\frac{1}{\rho_1 u_1^2}\int_0^\infty \rho u(u_1 - u)\, dy$

ϵ half-angle of cone

μ viscosity

ρ density

ϕ perturbation-velocity potential

Subscripts:

0 free-stream conditions

1 conditions at edge of boundary layer

b base

f friction

m maximum

REFERENCES

1. Allen, H. Julian: Estimation of the Forces and Moments Acting on Inclined Bodies of Revolution of High Fineness Ratio. NACA RM A9I26, 1949.

2. Jack, John R., and Burgess, Warren C.: Aerodynamics of Slender Bodies at Mach Number of 3.12 and Reynolds Numbers from 2×10^6 to 15×10^6. I - Body of Revolution with Near-Parabolic Forebody and Cylindrical Afterbody. NACA RM E51H13.

3. Chapman, Dean R.: An Analysis of Base Pressure at Supersonic Velocities and Comparison with Experiment. NACA TN 2137, 1950.

4. von Kármán, Theodor, and Moore, Norton B.: Resistance of Slender Bodies Moving with Supersonic Velocities, with Special Reference to Projectiles. Trans. A.S.M.E., vol. 54, no. 23, Dec. 15, 1932, pp. 303-310.

5. Luidens, Roger W., and Simon, Paul C.: Aerodynamic Characteristics of NACA RM-10 Missile in 8- by 6-Foot Supersonic Wind Tunnel at Mach Numbers from 1.49 to 1.98. I - Presentation and Analysis of Pressure Measurements (Stabilizing Fins Removed) NACA RM E50D10, 1950.

6. Chapman, Dean R., and Rubesin, Morris W.: Temperature and Velocity Profiles in the Compressible Laminar Boundary Layer with Arbitrary Distribution of Surface Temperature. Jour. Aero. Sci., vol. 16, no. 9, Sept. 1949, pp. 547-565.

7. Mangler, W.: Compressible Boundary Layers on Bodies of Revolution. VG 83, No. 47T, M.A.P. Volkenrode.

8. Crocco, Luigi: The Laminar Boundary Layer in Gases. Rep. CF-1038, Aerophysics Lab., North American Aviation, Inc., July 15, 1948.

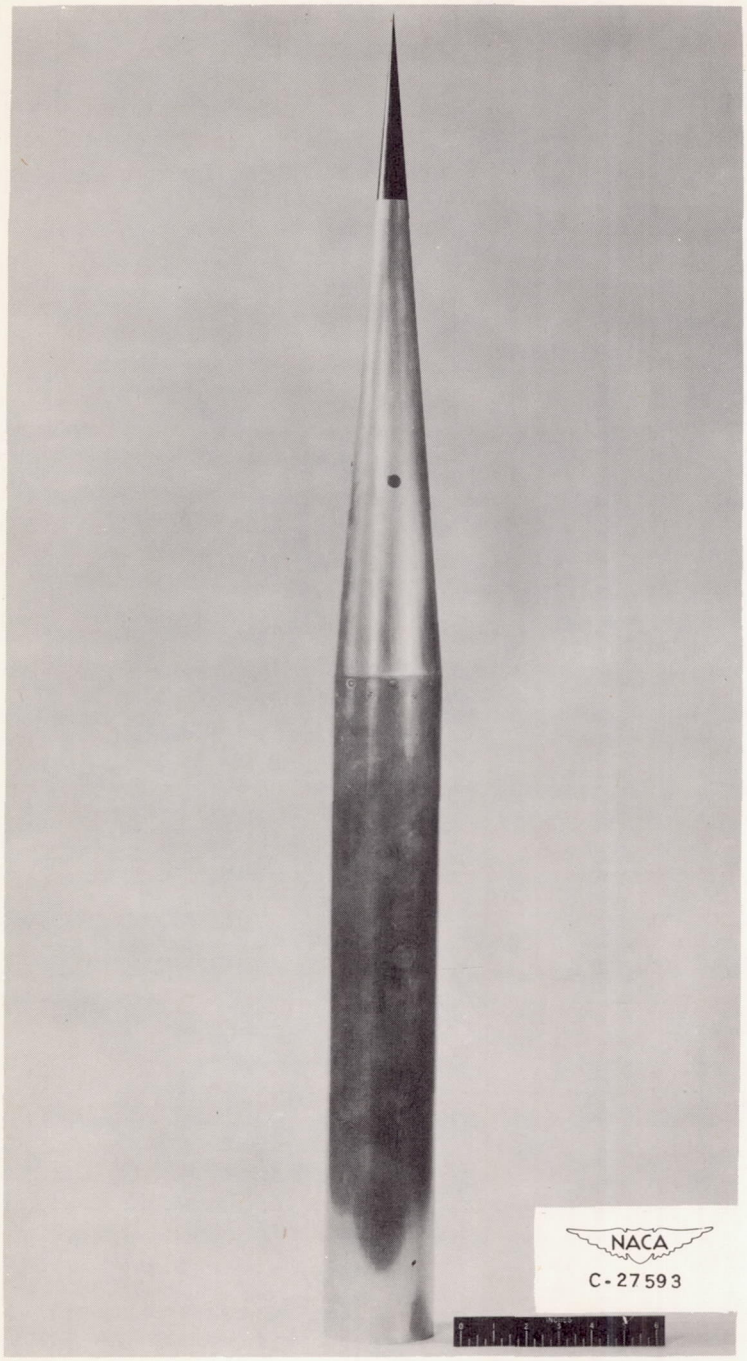

Figure 1. - Force model

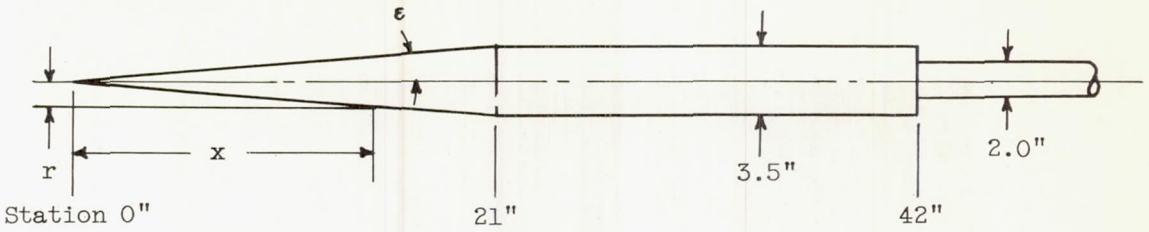

Model dimensions

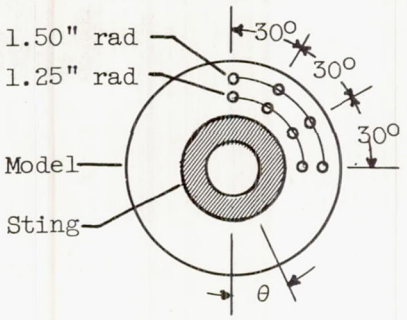

Base pressure orifices

Location of surface static-pressure orifices

x (in.)	θ (deg)				
	0	22.5	45	67.5	90
3	x				x
5	x	x	x	x	x
6	x				x
9	x				x
11	x	x	x	x	x
12	x				x
15	x				x
18	x				x
19	x	x	x	x	x
19.5	x				x
20	x				x
20.5	x				x
21.5	x				x

x (in.)	θ (deg)				
	0	22.5	45	67.5	90
22	x				x
22.5	x				x
23	x	x	x	x	x
25	x				x
27	x				x
29	x				x
31	x	x	x	x	x
33	x				x
35	x				x
37	x				x
39	x				x
41	x	x	x	x	x

Figure 2. - Schematic drawing of pressure-distribution model with location of static-pressure orifices.

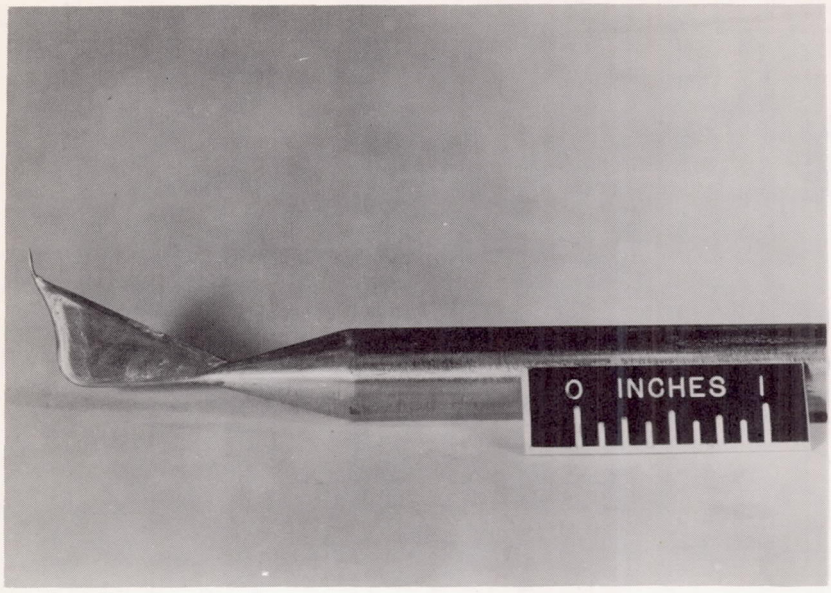

(a) Probe used to obtain boundary-layer data upstream of base.

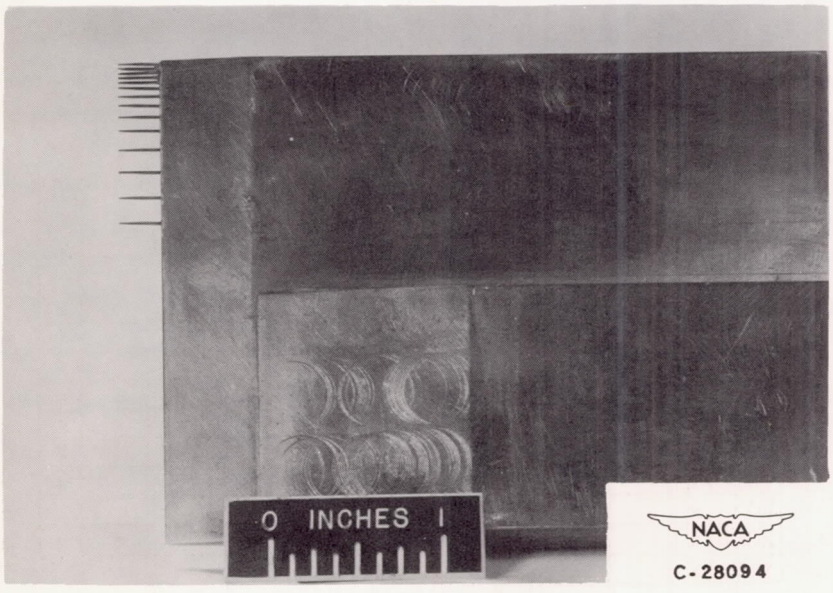

(b) Rake used to obtain boundary-layer data at base.

Figure 3. - Probe and rake used for boundary-layer surveys.

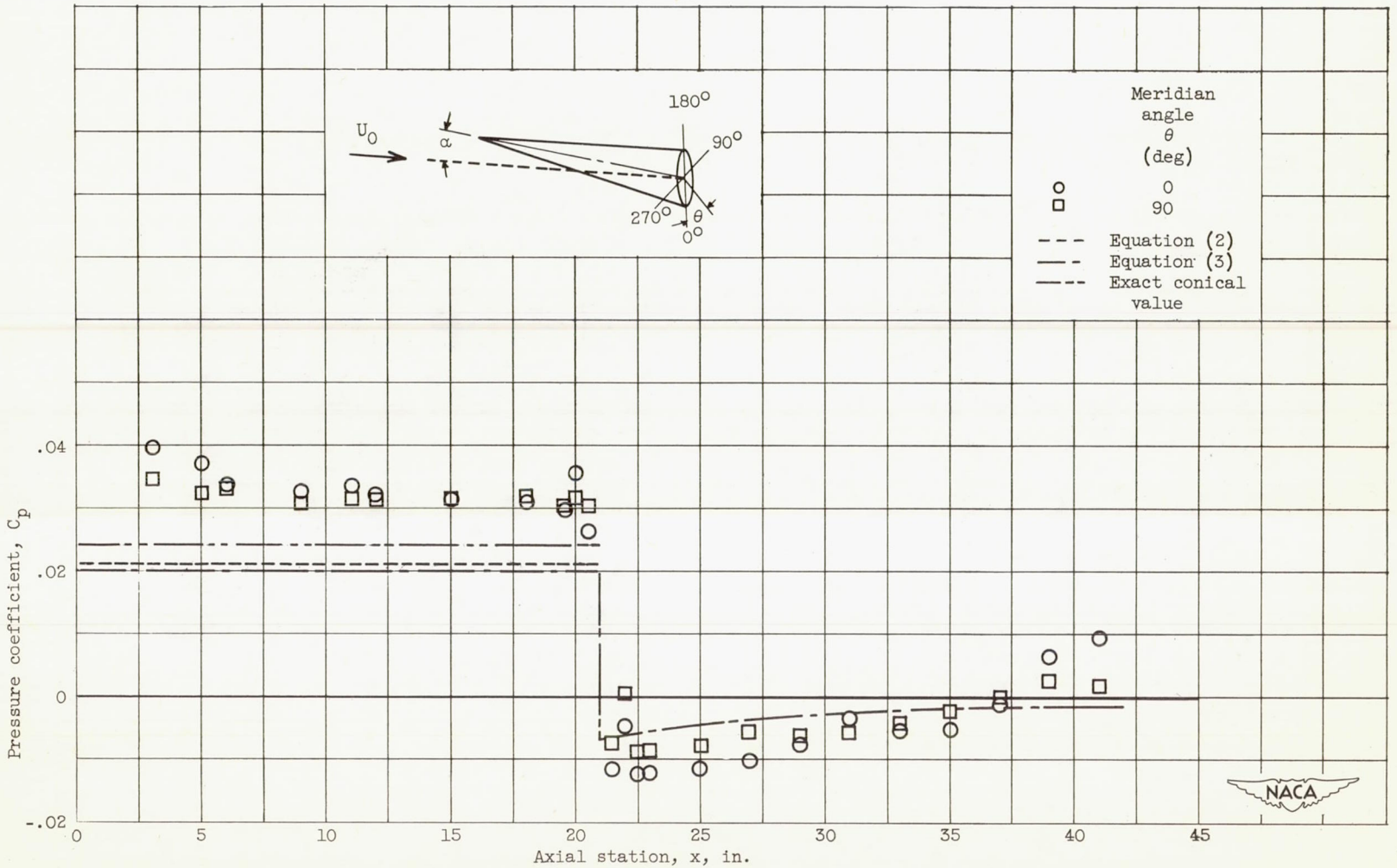

(a) Zero angle of attack.

Figure 4. - Experimental and theoretical axial variation of pressure coefficient.

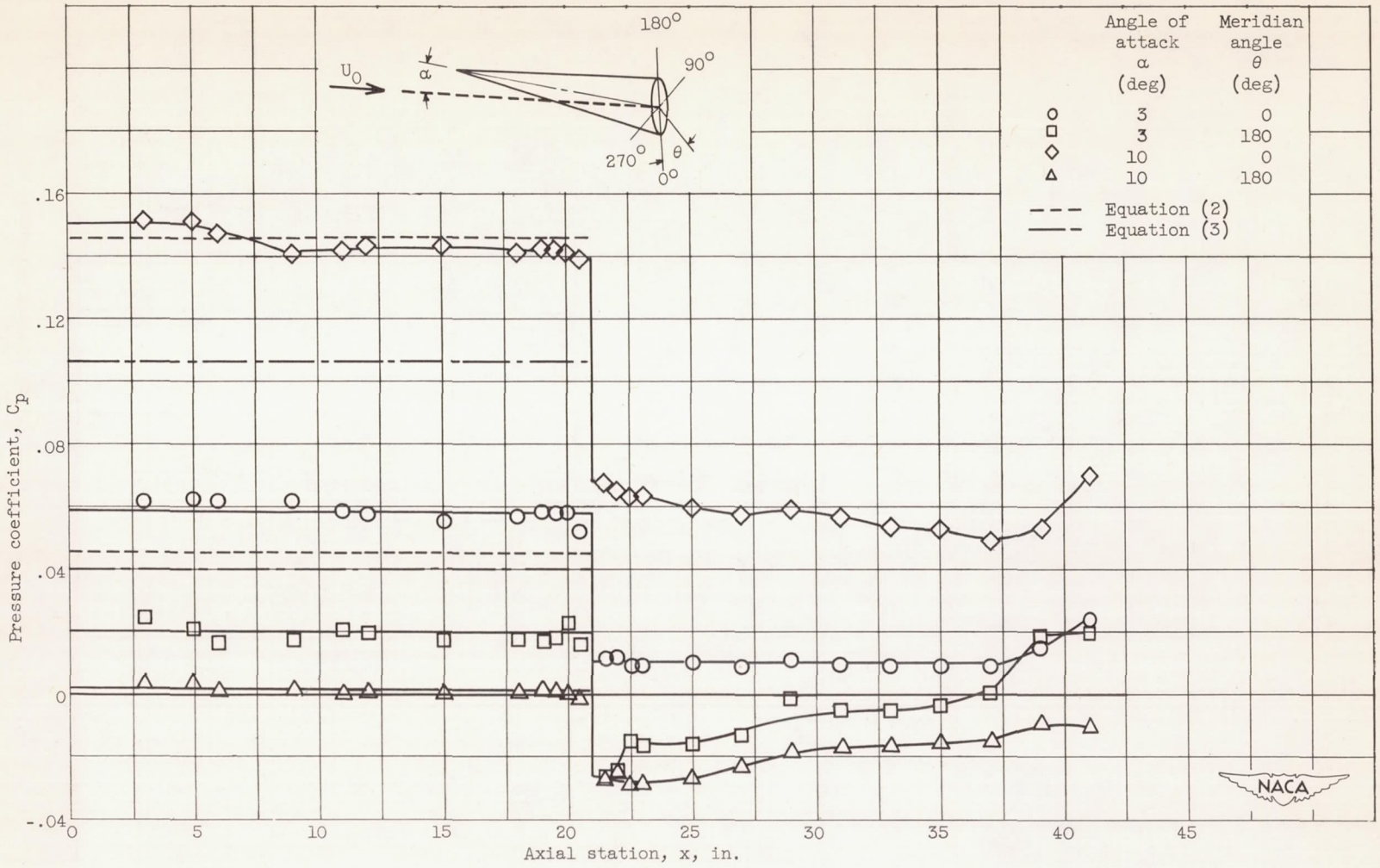

(b) Angles of attack of 3° and 10°.

Figure 4. - Concluded. Experimental and theoretical axial variation of pressure coefficient.

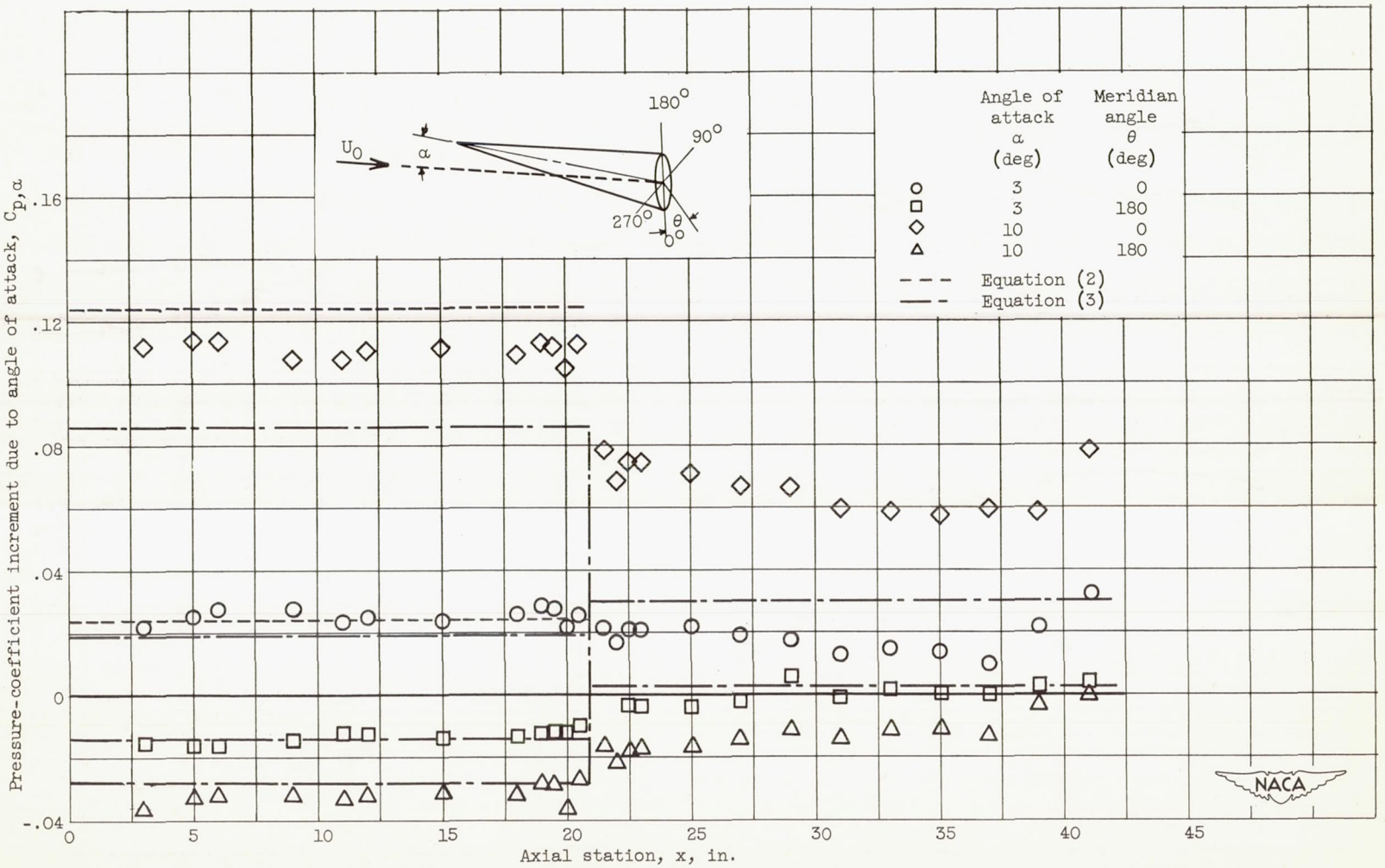

Figure 5. - Experimental and theoretical axial variation of pressure-coefficient increment due to angle of attack for two angles of attack.

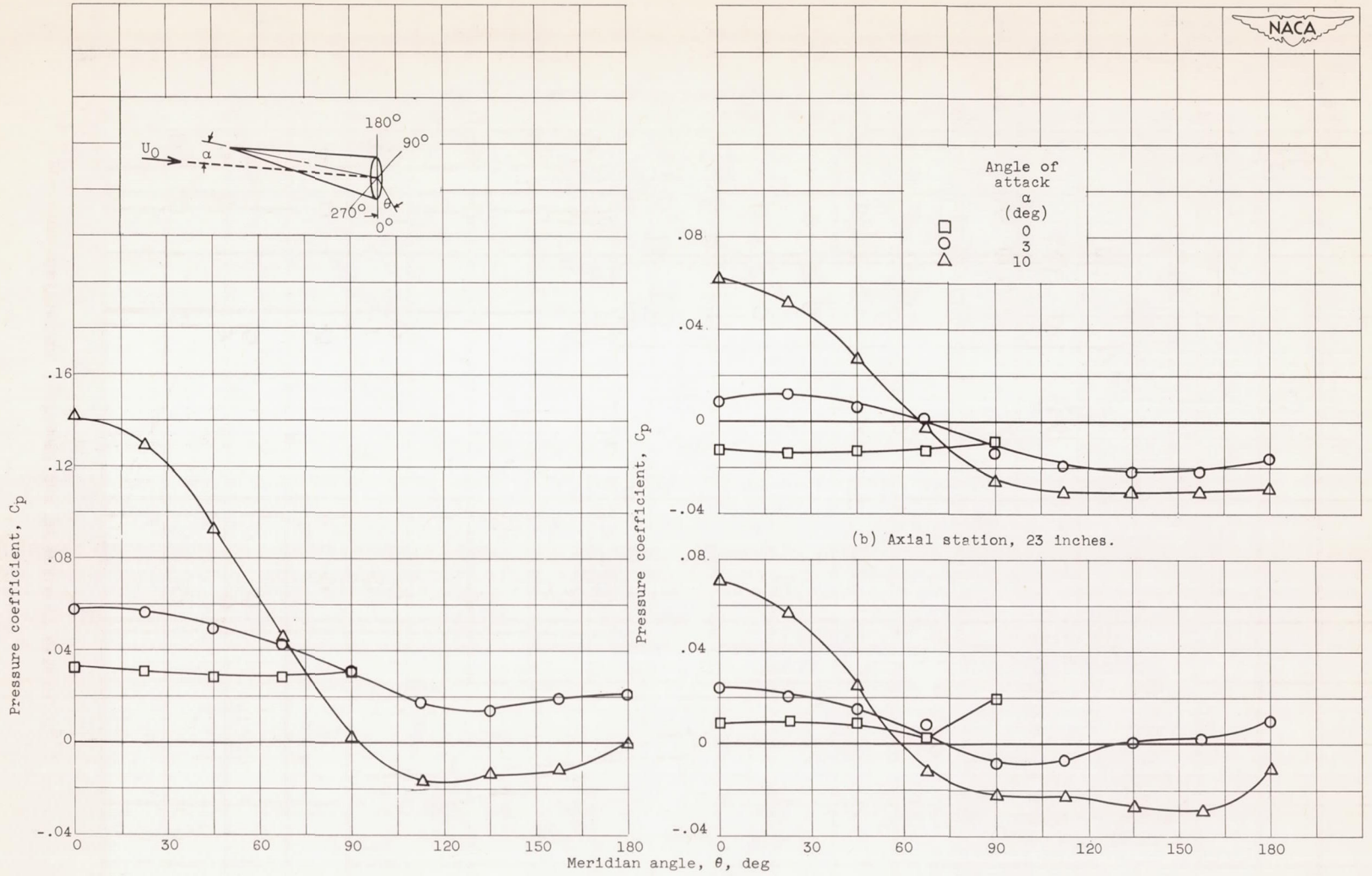

(a) Axial station, 11 inches.

(b) Axial station, 23 inches.

(c) Axial station, 41 inches.

Figure 6. - Variation of pressure coefficient at angle of attack with meridian angle.

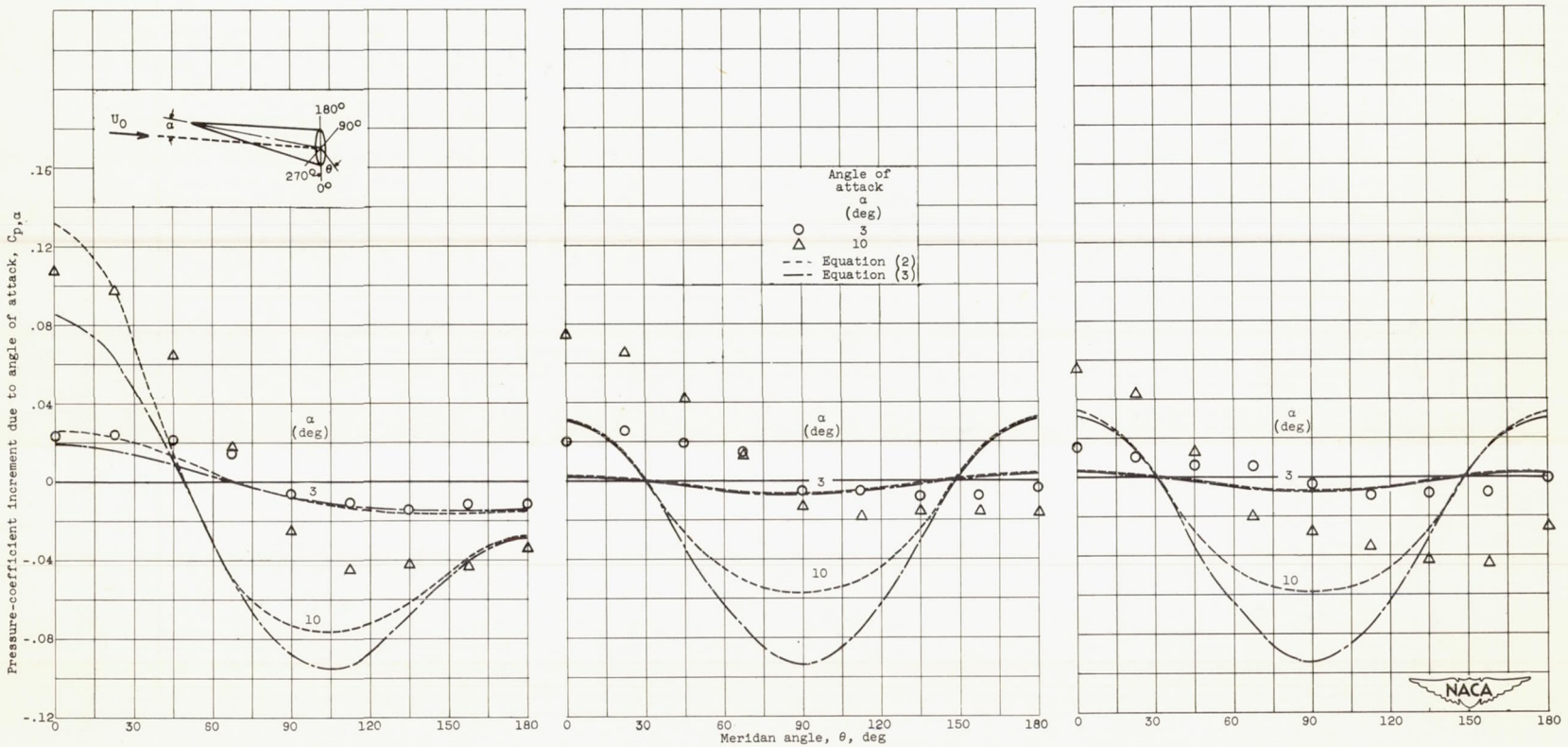

(a) Axial station, 11 inches. (b) Axial station, 23 inches. (c) Axial station, 41 inches.

Figure 7. - Variation of pressure-coefficient increment due to angle of attack with meridian angle.

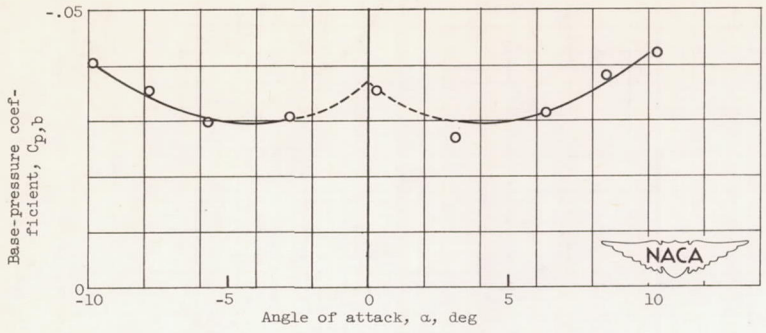

Figure 8. - Variation of base-pressure coefficient with angle of attack.

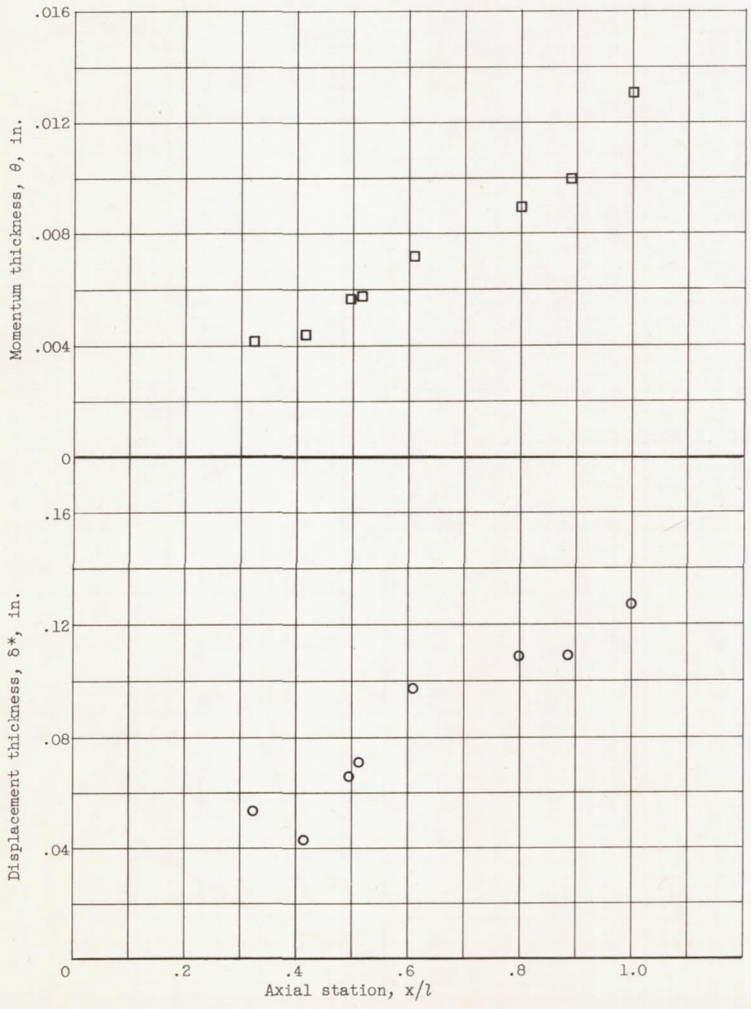

Figure 9. - Variation of displacement and momentum thicknesses with axial station.

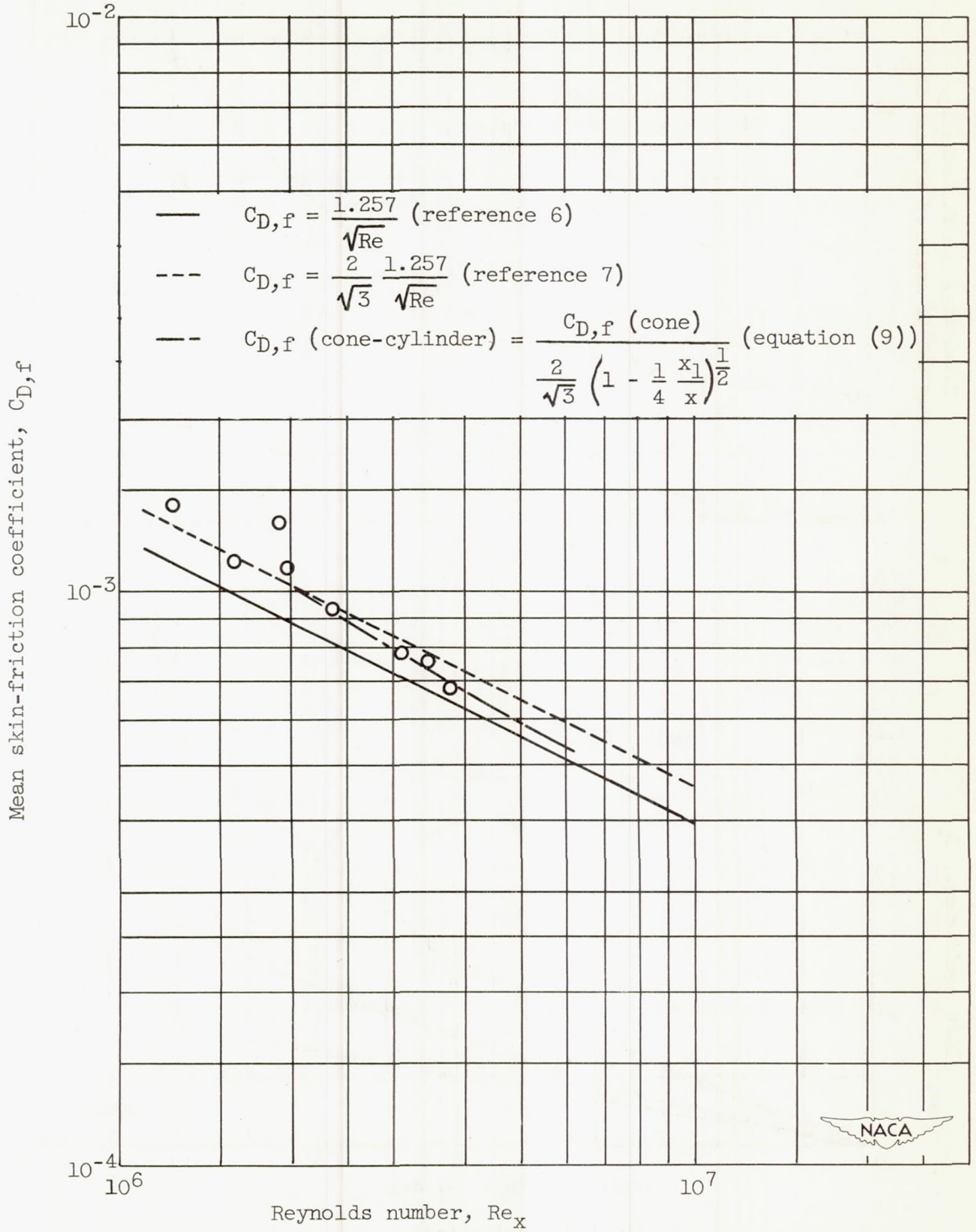

Figure 10. - Variation of mean friction-drag coefficient with Reynolds number for zero angle of attack.

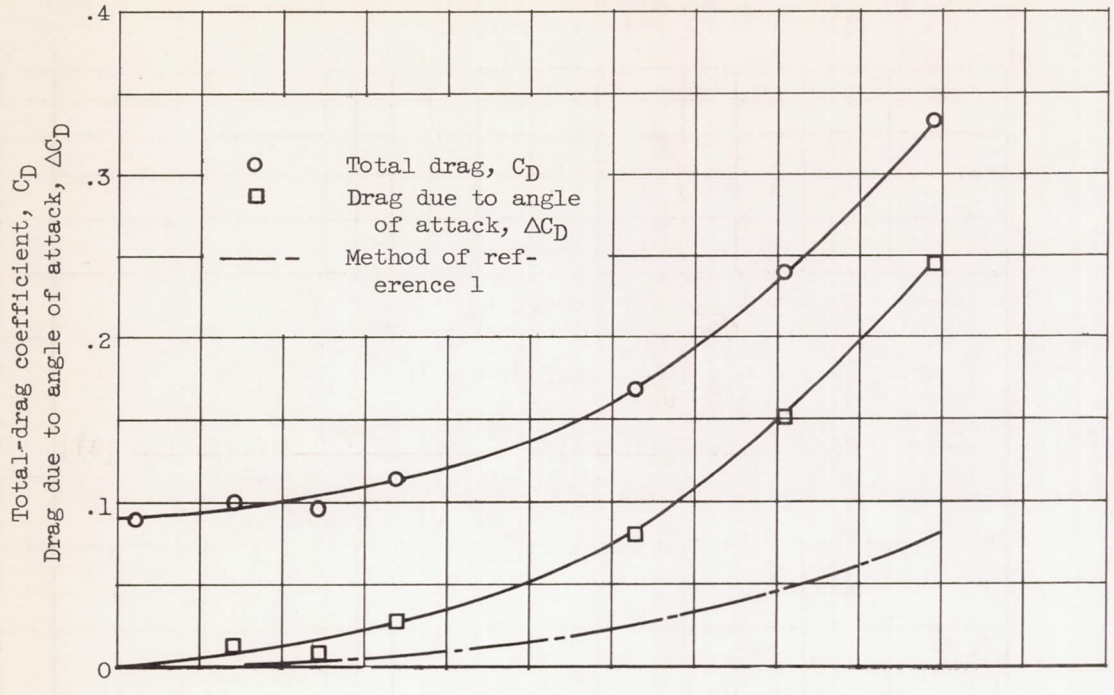

(a) Drag coefficient.

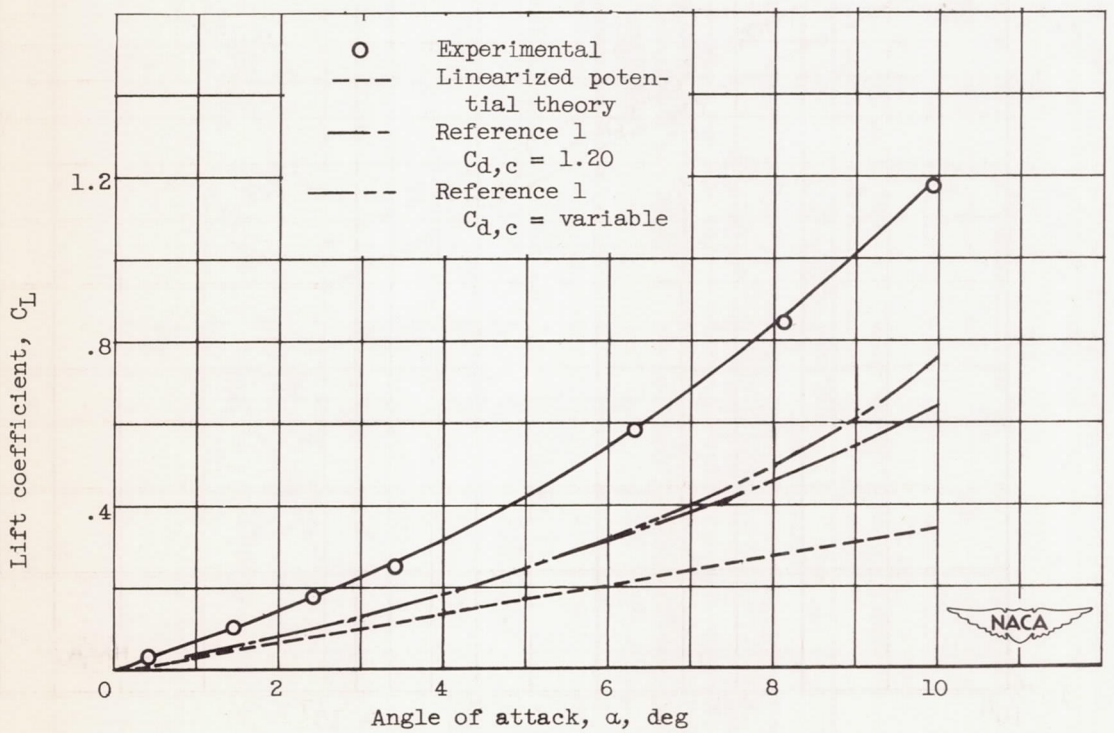

(b) Lift coefficient.

Figure 11. - Variation of aerodynamic characteristics with angle of attack.

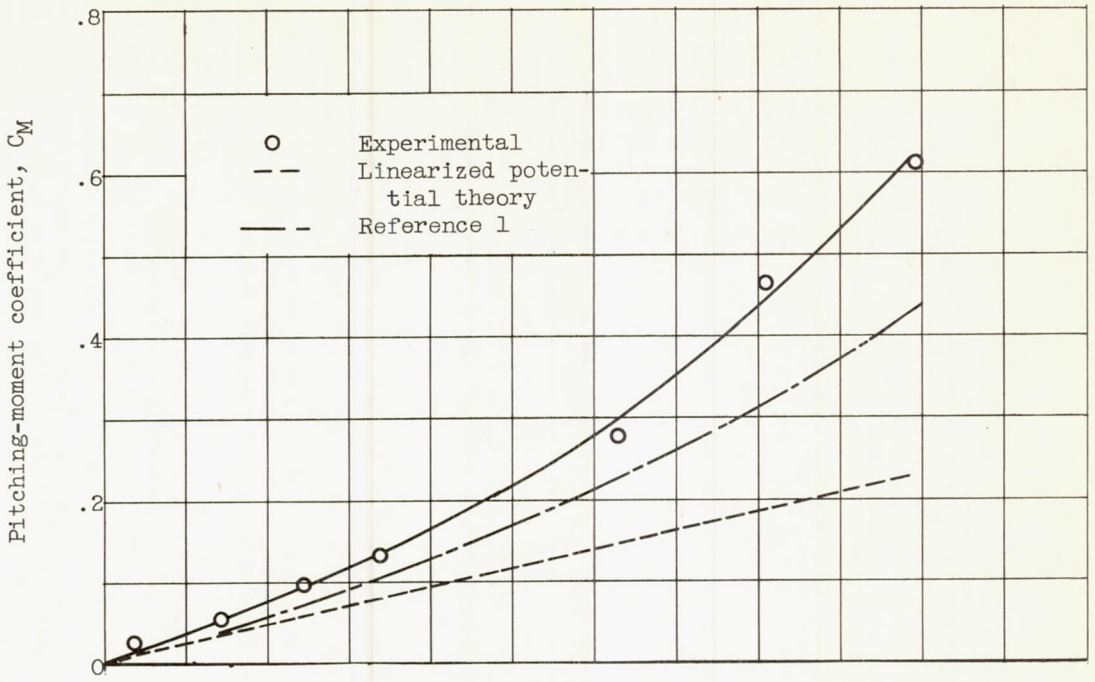

(c) Pitching-moment coefficient.

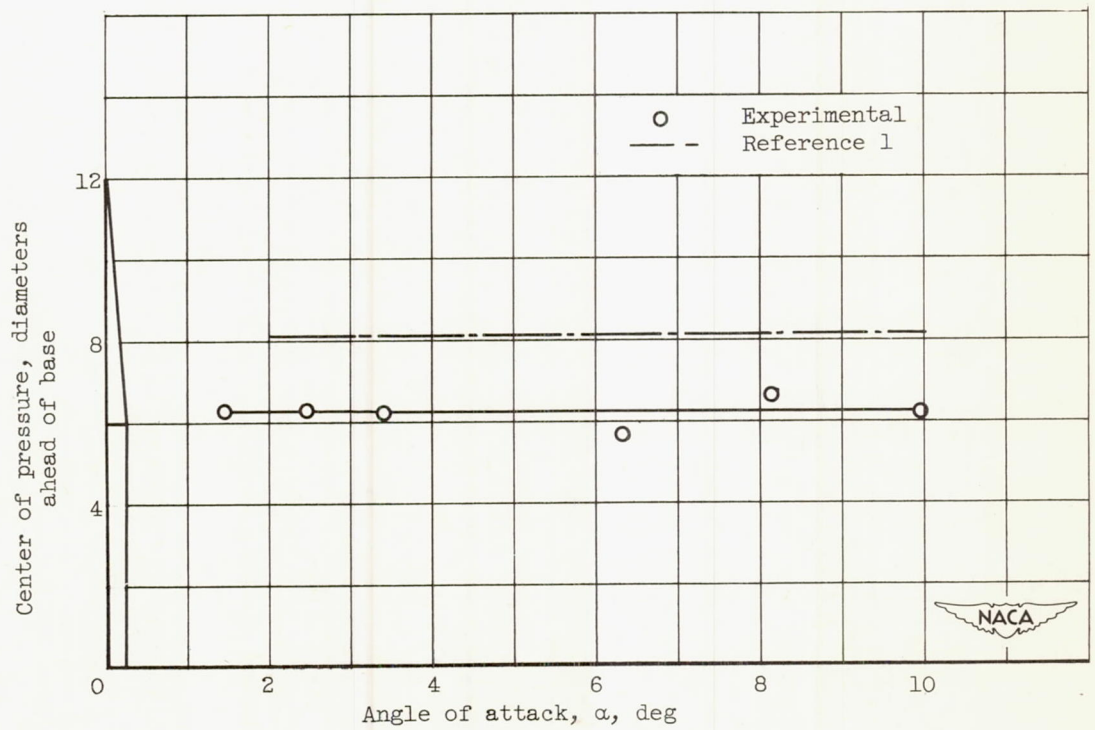

(d) Center of pressure.

Figure 11. - Concluded. Variation of aerodynamic characteristics with angle of attack.